ADVANCED FUNCTIONAL MATERIALS
www.afm-journal.de

Materials Views
www.MaterialsViews.com

Manganese Oxide Octahedral Molecular Sieves (OMS-2) Multiple Framework Substitutions: A New Route to OMS-2 Particle Size and Morphology Control

*Cecil K. King'ondu, Naftali Opembe, Chun-hu Chen, Katana Ngala, Hui Huang, Aparna Iyer, Hector F. Garcés, and Steven L. Suib**

Self-assembled multidoped cryptomelane hollow microspheres with ultrafine particles in the size range of 4–6 nm, and with a very high surface area of 380 $m^2 g^{-1}$ have been synthesized. The particle size, morphology, and the surface area of these materials are readily controlled via multiple framework substitutions. The X-ray diffraction and transmission electron microscopy (TEM) results indicate that the as-synthesized multidoped OMS-2 materials are pristine and crystalline, with no segregated metal oxide impurities. These results are corroborated by infrared (IR) and Raman spectroscopy data, which show no segregated amorphous and/or crystalline metal impurities. The field-emission scanning electron microscopy (FESEM) studies confirm the homogeneous morphology consisting of microspheres that are hollow and constructed by the self-assembly of pseudo-flakes, whereas energy-dispersive X-ray (EDX) analyses imply that all four metal cations are incorporated into the OMS-2 structure. On the other hand, thermogravimetric analyses (TGA) and differential scanning calorimetry (DSC) demonstrate that the as-synthesized multidoped OMS-2 hollow microspheres are more thermally unstable than their single-doped and undoped counterparts. However, the in-situ XRD studies show that the cryptomelane phase of the multidoped OMS-2 hollow microspheres is stable up to about 450 °C in air. The catalytic activity of these microspheres towards the oxidation of diphenylmethanol is excellent compared to that of undoped OMS-2 materials.

1. Introduction

The mixed valence framework and tunnel structure of cryptomelane-type (KMn_8O_{16}) manganese oxide octahedral molecular sieves[1] (OMS-2) are characteristics of this unique class of inorganic systems whose particle size, unit cell system, and morphology can be tuned via subtle introduction of ions into their tunnels, and/or by using their mixed valence framework as a solid solution to 'dissolve' a wide variety of metal ions. Thus, nanoscale OMS-2 materials can be generated with novel/superior chemical and physical properties compared to those of their macroscale counterparts. These novel properties of nanoscale materials have been attributed to their size and morphology. In nanoscale materials, the ratio of the number of superficial atoms in their particles to the number in the bulk is much larger than that in macroscale materials, and this gives rise to their novel properties.[2]

Because of the strong size/morphology-property correlation upheld by nanotechnology, coupled with their (OMS-2 materials) current wide-ranging embryonic applications in gas cleansing, separation, batteries, catalysis, and chemical sensing,[3–7] a fair amount of attention has recently been paid towards tailoring their crystal system, particle size, and morphology. To realize this, a considerable number of strategies including manipulation of temperature, pressure, time, and pH under hydrothermal[8–10] and reflux[11] conditions, as well as the use of co-solvents,[11] sols,[12–14] catalysts,[15] and reducing agents[16,17] have been explored.

In addition, the introduction of single-type ions into the tunnels and in the mixed-valent framework of cryptomelane, in an effort to modify its properties, has been undertaken. For example, partial exchange of K^+ ions in the K-OMS-2 tunnels with H^+ ions (protons) has yielded excellent acid catalysts for selective oxidation reactions,[18] whereas doping of single-type, low-, or high-valent metal cations, such as Co^{2+}, Zr^{2+}, Cu^{2+}, Cr^{3+}, Fe^{3+}, In^{+3}, V^{5+}, W^{6+}, and Mo^{6+} into the framework,[19–25] via a subtle balance of the redox properties and depending on the extent of substitution, has produced cryptomelane with novel morphologies[26] and catalytic properties.[27] In terms of morphology, doping Cr^{3+} into the K-OMS-2 structure produced well-ordered dendritic structures, which are unusual compared to the regular K-OMS-2 morphology.[26]

C. K. King'ondu, N. Opembe, C.-H. Chen, K. Ngala, H. Huang, A. Iyer, Prof. S. L. Suib
Department of Chemistry
University of Connecticut
55 North Eagleville Road, Storrs, CT 06269–3060, USA
E-mail: steven.suib@uconn.edu
H. F. Garcés, Prof. S. L. Suib
Institute of Materials Science
University of Connecticut
55 North Eagleville Road, Storrs, CT 06269, USA

DOI: 10.1002/adfm.201001020

Although single framework substitution has been reported, multiple framework substitutions to the best of our knowledge have not. Moreover, synthetic cryptomelane has until now been reported to invariably crystallize into a tetragonal crystal system that gives rise to its quintessential fibrous/nanorod morphology.

Herein, we report a facile synthesis of novel, multidoped cryptomelane self-assembled hollow microspheres; the first multiple substitutions to have been done without compromising the mixed valency, porosity, and crystalline nature of OMS-2 materials. Unlike in other reported OMS-2 syntheses, multidoping was herein used to dramatically control the particle size, morphology, and the surface area. The self-assembled multidoped OMS-2 hollow microspheres reported in this work were obtained by a template/surfactant-free reaction between potassium permanganate and manganese (II) sulfate, with sodium molybdate, vanadyl, copper, and iron sulfate acting as the source of Mo, V, Cu, and Fe dopant cations, respectively.

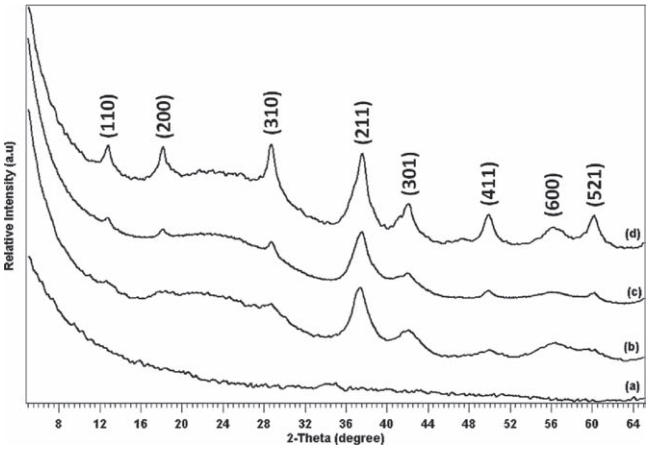

Figure 2. XRD patterns of multidoped OMS-2 prepared with and without acid. a) 15% total dopants with acid, b) 15% without acid, c) 10% with acid, d) 10% without acid. Reaction conditions: 24 h refluxing time at 100 °C.

2. Results

2.1. X-ray Diffraction

X-ray diffraction (XRD) was used to identify the phase of the products; to determine the effect of nitric acid on the crystallization of multidoped OMS-2; to determine the maximum total amount of dopants (in percent weight of the total manganese) permissible for the formation of crystalline multidoped OMS-2; and to verify the success of multiple framework substitutions as well as determining the effect of each metal cation on the overall particle size of the multidoped OMS-2 materials. Orientation of tunnels and corresponding TEM electron beams are shown in **Figure 1**. As shown in **Figure 2**, the diffraction pattern for the sample with 10% total amount of dopants (Figure 2d), showed peaks which could be indexed to the pure cryptomelane phase (space group ($I4/m$) with unit cell parameters; $a = b =$ 9.815 Å and $c = 2.847$ Å. No additional peaks corresponding to segregated crystalline phases of Fe, Cu, V, and Mo oxides were observed, indicating that the multidoped OMS-2 crystallized as a pure phase.

In order to investigate the influence of nitric acid (HNO_3) on the crystallization of the multidoped OMS-2 materials, 10% and 15% (w/w) multidoped OMS-2 samples were each prepared by refluxing the precursors for 24 h at 100 °C with and without the acid. As shown by the XRD patterns (Figure 2), nitric acid was found to dramatically influence the crystallinity of multidoped OMS-2. The samples that had been prepared without the acid, see Figure 2b and 2d, were found to be relatively more crystalline than those prepared with the acid. This phenomenon has not been reported for the syntheses of either undoped or single-metal doped cryptomelane. Based on the effect of nitric acid on the crystallization of multidoped OMS-2 materials, the maximum total amount of dopants permissible for the formation of crystalline multidoped OMS-2 was determined by synthesizing–without nitric acid–samples with different total amounts of dopants. As shown by the XRD patterns in **Figure 3**, the maximum total amount of dopants allowable was found to be 15% (w/w) of the total manganese. Decreasing the total amount of dopants from 15% to 10% markedly increased the XRD peak intensities, and also decreased their widths, Figure 3c. On the other hand, increasing the total amount of dopants beyond 15% led to an amorphous phase (Figure 3a).

In order to verify the success of multiframework substitution and to determine the effect of each metal cation on the overall crystallite size of the multidoped OMS-2, one metal dopant at a time was excluded from the recipe for synthesizing a 10% multidoped OMS-2 material. X-ray diffraction and the Debye–Scherrer equation[28] were then used to follow changes in the crystallite size. As shown by the XRD patterns in **Figure 4**, the crystallite size increased from 4.0 nm when all four dopants were present, to 5.0 nm, 6.0 nm, 7.0 nm, and 29.0 nm when Fe, Cu, V, and Mo, respectively, were omitted from the recipe.

Other than the total amount of dopants and the presence of nitric acid, the refluxing time was found to profoundly influence the crystallization of multidoped OMS-2. All the samples prepared by refluxing for 24 h, 48 h, and 72 h showed pure cryptomelane phases (see XRD patterns in the Supporting Information, Figure S1). However, marked differences in peak widths and intensities were observed. As shown in Figure S1, increasing the refluxing time decreased the XRD peak

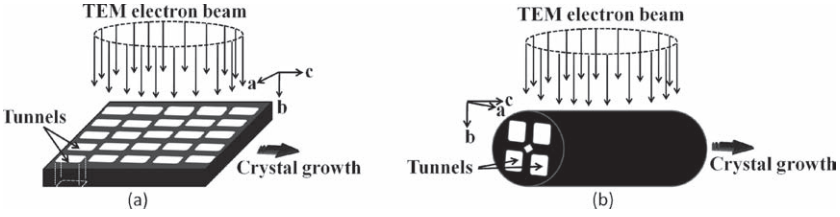

Figure 1. Schematic illustration of the most probable orientation of the tunnels in different particles, with respect to the TEM electron beam. a) Flake-like particle with distorted tetragonal crystal structure. b) Fiber-like particle with tetragonal crystal structure.

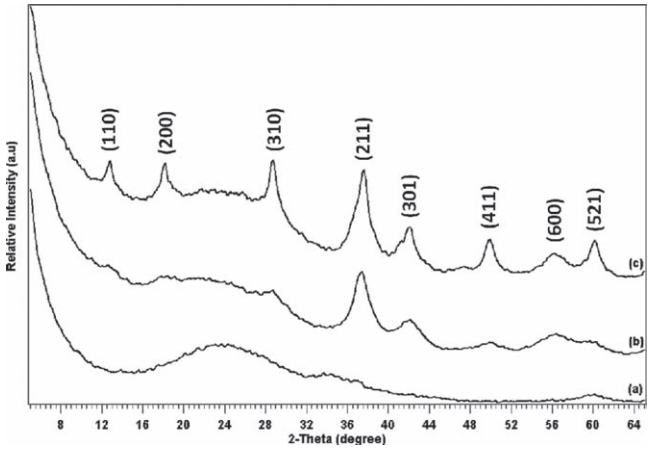

Figure 3. XRD patterns of multidoped OMS-2 prepared at different total dopants levels: a) 20%, b) 15%, and c) 10%. (Initial concentration: at each percentage level, all four dopants were of equal amount in weight (2.5%)). Reaction conditions: 24 h refluxing time at 100 °C without acid.

widths and increased their intensities. The crystallite sizes of the samples refluxed for 24 h, 48 h, and 72 h–calculated by the Debye–Scherrer equation–were 4.0 nm, 6.0 nm, and 9.0 nm, respectively.

2.2. Field-Emission Scanning Electron Microscopy

Morphological studies on the as-synthesized products were conducted by transmission electron microscopy (TEM) and field-emission scanning electron microscopy (FESEM). As shown in **Figure 5**, all the samples (prepared with and without nitric acid) showed three degrees of hierarchy: primary structures (1°), secondary structures (2°), and tertiary structures (3°). The primary structures consist of ultrafine, tunnel-laden crystals with interplanar spacings of 4.57 Å and 6.7 Å, whereas the secondary structures are pseudo-flakes shown in Figure 5b inset, and in **Figure 6**a,b. The tertiary structures on the other hand, are

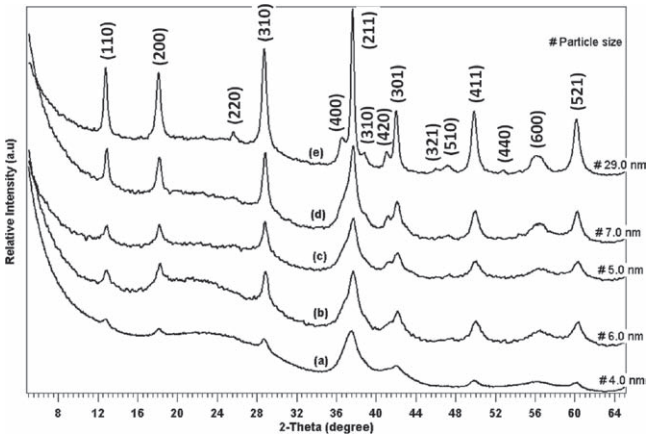

Figure 4. XRD patterns of multidoped OMS-2: a) doped with Mo, V, Fe, and Cu, b) doped with Mo, V, and Fe, c) doped with Mo, V, and Cu, d) doped with Mo, Fe, and Cu, e) doped with V, Fe, and Cu. Reaction conditions: 24 h refluxing time at 100 °C under acidic conditions.

self-assembled hollow microspheres with an average diameter of 0.5–2.0 μm, Figure 5. The hollow nature of the microspheres is evident from Figure S2 in the Supporting Information, and also from Figure 5d, which shows a broken microsphere exposing its cavity, and two more microspheres with open holes.

2.3. Transmission Electron Microscopy

The formation of multidoped cryptomelane was confirmed by crystal structure studies carried out by TEM. As shown in Figure 6b and the Supporting Information (Figure S4), crystalline multidoped OMS-2 nanoparticles with an average size of about 5.0 nm were obtained. A high-resolution TEM (HRTEM) image (Figure 6c) of a nanoparticle in Figure 6b shows that the particle is structurally single crystalline with periodic lattice fringes of 4.57 Å corresponding to the interplanar spacing of (002) planes. Figure 6f also shows a particle exposing (101) planes, which is evident by periodic lattice fringes of 6.7 Å, as shown in Figure 6g. The interplanar spacings observed are all in accordance with those measured with XRD for the bulk powder sample.

Consistent with the work of Villegas et al.[16] the characteristic tunnel structure of cryptomelane is manifested in our material, see HRTEM image in Figure 6e. However, unlike other observations of these reported tunnels, 1×1 and 2×2 tunnels, which for a very long time have only been observed in simulated structures of OMS-2, have now been confirmed experimentally for the first time, see top-right inset of Figure 6e. The tunnels observed in our synthesized multidoped OMS-2 material are akin to the ones in the simulated OMS-2 structure (top-left inset of Figure 6e) drawn with CrystalMaker.[29]

2.4. Raman and Fourier-Transform Infrared Spectroscopy (FTIR)

The lattice vibrational behavior of both the undoped and 10% multidoped OMS-2 materials was studied with FTIR and Raman spectroscopy in order to probe the effect of multiple substitution(s) on the spectral features of the OMS-2 materials and check for the presence of segregated crystalline and/or amorphous metal oxides.

To study the effects of multidoping, we first studied the lattice behavior of undoped and single-metal doped OMS-2 materials. As shown in the Supporting Information (Figure S4), the FTIR spectrum of the as-synthesized regular OMS-2 material shows features similar to those previously reported;[30] namely, absorption bands at around 720 cm^{-1}, 590 cm^{-1}, 530 cm^{-1}, and 470 cm^{-1}. Upon single-doping of Mo and V into the OMS-2 structure, the band at 590 cm^{-1} slightly increased in intensity, whereas the one at 470 cm^{-1} decreased in intensity, Figure S4(c) and (e). However, doping with Fe and Cu did not change the peak intensities significantly. Multiple-doping on the other hand, produced a dramatic increase in the intensity of the peak at 590 cm^{-1} as well as a significant decrease in the intensity of the peak at 470 cm^{-1}, **Figure 7**.

In addition to probing lattice vibrational behavior, FTIR, because of its sensitivity towards amorphous, short-range and long-range order materials,[31] was also used to check for

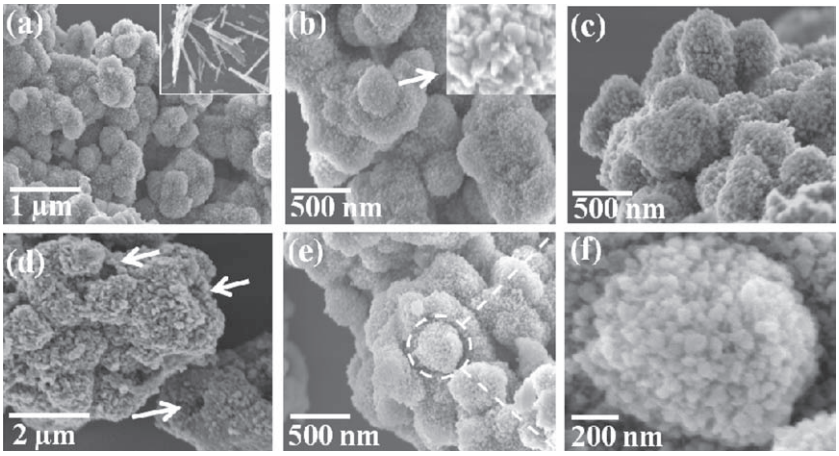

Figure 5. FESEM of 10% multidoped OMS-2: a,b,e) prepared without acid for 24 h at 100 °C, c) prepared with acid for 24 h at 100 °C, d) prepared with acid for 72 h at 100 °C. The arrows in (d) show two microspheres with holes and a broken microsphere exhibiting its hollow structure. f) Magnified hollow microsphere. The inset in (a) shows the image of regular K-OMS-2 prepared for 24 h at 100 °C.

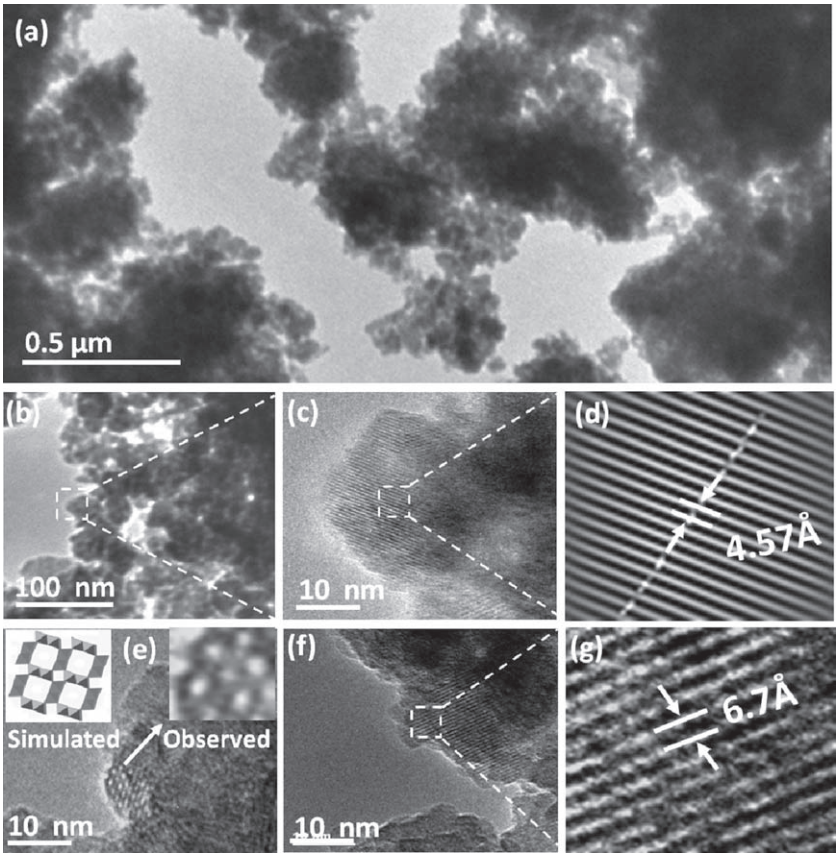

Figure 6. HRTEM of 10% multidoped OMS-2 prepared without acid for 24 h at 100 °C. a) General flake-like morphology of synthesized 10% multidoped OMS-2 materials. b) Separated particles from collapsed microsphere after vigorous sonication. c) A nanoparticle showing (200) lattice fringes. d) Inverse Fourier-transform pattern of (110) lattice fringes. e) Manifestation of tunnel structure of the nanocrystals: Top right and top left insets show 1×1 and 2×2 tunnels of the simulated and observed cryptomelane f) A nanoparticle showing (110) lattice fringes. g) Magnified (110) lattice fringes.

the probable segregated amorphous Fe, Cu, V, and Mo oxide impurities in the as-synthesized 10% multidoped OMS-2 materials, which, if present, would not have been detected by XRD. As shown in Figure S5 in the Supporting Information, no segregated metal oxide impurities were detected (in any appreciable amount), in the 10% multidoped OMS-2 material prepared without acid.

The Raman data, **Figure 8**, features six characteristic peaks at around 750 cm^{-1}, 650 cm^{-1}, 580 cm^{-1}, 530 cm^{-1}, 480 cm^{-1}, and 380 cm^{-1} for the regular K-OMS-2 as opposed to only four peaks at around 750 cm^{-1}, 650 cm^{-1}, 580 cm^{-1}, and 530 cm^{-1} that were found for the 10% multidoped OMS-2 material. The four Raman peaks at around 750 cm^{-1}, 650 cm^{-1}, 580 cm^{-1}, and 530 cm^{-1} are relatively sharper and more intense for the regular K-OMS-2 (Figure 8a) than for the 10% multidoped material, Figure 8b.

The Raman spectra, with respect to the crystallinity, are in good agreement with the structural data obtained by XRD for the same materials. In addition, with regards to impurities, the major peaks of MoO_3,[32] V_2O_5,[33] Fe_2O_3,[34] and CuO[35] at 820 cm^{-1}, 993 cm^{-1}, 1323 cm^{-1}, and 289 cm^{-1}, respectively, were not observed in the Raman spectrum (Figure 8b) of the 10% multidoped OMS-2 material.

2.5. Surface Area and Pore-Distribution Analysis

The N_2 adsorption/desorption isotherms, pore distribution, and surface areas of the undoped, single-doped, and the 10% multidoped OMS-2 materials were acquired using a Micromeritics instrument, and the surface areas and pore distributions in the mesopore/micropore regions were calculated using the Brunauer-Emmett-Teller (BET) and Barrett-Joyner-Halenda (BJH) methods, respectively. The N_2 adsorption/desorption isotherms of the 10% multidoped OMS-2 materials, **Figure 9**, show fairly large hysteresis loops in the P/P_0 range above 0.45, and a rapid increase in the volume of adsorbed gas at relative pressures P/P_0 greater than 0.5. These N_2 adsorption/desorption isotherms and their corresponding hysteresis loops (Figure 9) are quite different from those reported for regular OMS-2.[11,36] The observed hysteresis loops occur at relatively low P/P_0 (0.45–0.8) values that are far from saturation, compared to the reported hysteresis loops,[11,36] which occur at P/P_0 values close to saturation. In

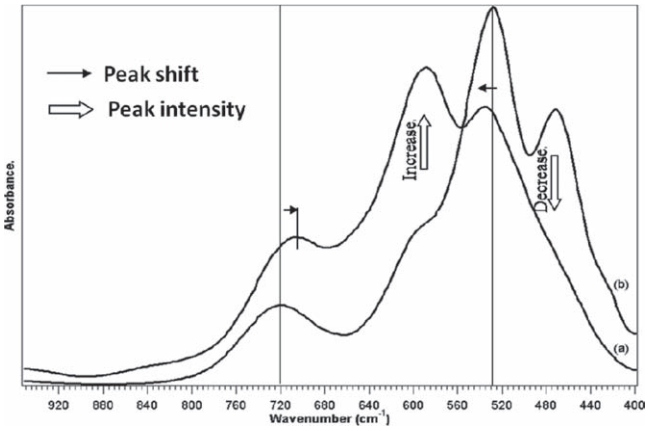

Figure 7. FTIR spectra of a) 10% multidoped OMS-2 prepared under acidic conditions at 100 °C, b) K-OMS-2 prepared under acidic conditions.

addition, the N_2 adsorption/desorption isotherms of the 10% multidoped OMS-2 materials (doped with four metal cations) and their hysteresis loops are quite different from those of OMS-2 materials doped with three metal cations, see the Supporting Information, Figure S6.

The BET surface area for the single-doped OMS-2 materials was found to be higher for the high valent metal ions (Mo^{6+} and V^{5+}) than for the low valent metal ions (Cu^{2+} and Fe^{2+}), see Supporting Information, Table S7. Consistent with the BET surface area results for the single-doped OMS-2 materials, the surface areas of the multidoped OMS-2 materials were higher when Mo and V cations were both present in the synthesized materials, and lower when either of them was absent in the multidoped OMS-2 materials, Table S7. These results match the XRD data (Figure 4) in terms of the particle size, as the omission of Mo and V cations in the synthesis of the multidoped OMS-2 material leads to a significant increase in particle size, which is accompanied by a decrease in the surface area.

When all four metal cations were present in the multidoped OMS-2 materials, the BET surface area increased dramatically to 380 and 367 $m^2\ g^{-1}$ for 10% multidoped OMS-2 materials

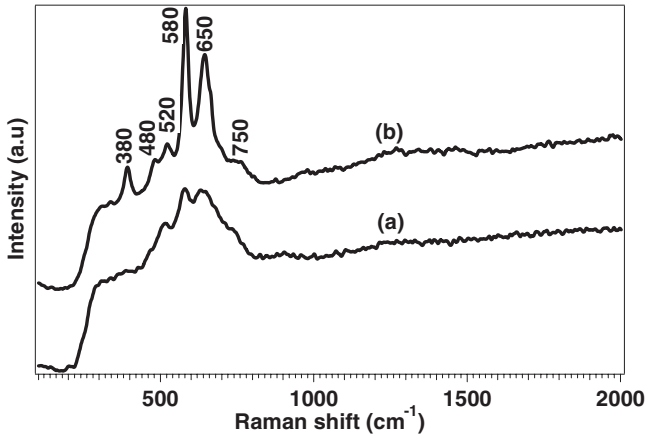

Figure 8. Raman spectra of a) 10% multidoped OMS-2 prepared without nitric acid and b) regular K-OMS-2. *Reaction conditions:* 24 h refluxing time at 100 °C.

synthesized with and without nitric acid, respectively. These are the highest BET surface areas (367 and 380 $m^2\ g^{-1}$) reported for synthetic cryptomelane to date. The micropore volumes of the 10% multidoped OMS-2 materials were found to be higher than those of the OMS-2 materials doped with three metal cations, as well as the reported micropore volumes of the undoped and single-doped OMS-2,[36] see **Table 1** for surface area, pore size, micropore, and mesopore volumes.

2.6. Energy Dispersive X-Ray Analysis

Elemental analyses of the undoped and the 10% multidoped OMS-2 materials were carried out by energy-dispersive X-ray spectroscopy (EDAX), and the results are summarized in **Table 2**.

As shown in Table 2, all four dopants: V, Mo, Fe, and Cu were present in the as-synthesized 10% multidoped OMS-2 material.

The atomic weight percentages of the V and Mo in the as-synthesized 10% multidoped OMS-2 were both close to the initial calculated value of 2.5%, whereas that of Cu and Fe were smaller and greater, respectively, than their calculated values. Table 2 also shows that the amount of K in the 10% multidoped OMS-2 was almost half the amount of that in the undoped K-OMS-2. Close examination of the local chemical environment of the sample represented by four spots in the EDAX data shows that the amount of each element (Mn, K, Cu, Fe, Mo, and V) in the 10% multidoped OMS-2 material remained relatively the same in the four regions.

2.7. Thermal Stability and Phase Change

The thermal stability of the synthesized 10% multidoped materials was studied using thermogravimetric analysis (TGA) and differential scanning calorimetry (DSC) under nitrogen atmosphere and compared to that of the regular OMS-2 and single-doped OMS-2 materials. As shown in **Figure 10**, four major weight losses were observed in the TGA profiles of both the regular OMS-2 and single-doped OMS-2 materials, as opposed to only three major weight losses observed in the TGA profiles of the 10% multidoped OMS-2 materials prepared with and without nitric acid. The regular OMS-2 (Figure 10g) was found to be more thermally stable than its single-doped and multi-doped counterparts.

Upon multidoping, the thermal stability of OMS-2 was found to drop sharply, as shown by the rapid weight losses exhibited by the 10% multidoped OMS-2 materials, Figure 10a and 10b. The first weight loss (ca. 7%) for the 10% multidoped OMS-2 materials prepared with and without nitric acid was observed between 35–120 °C. This weight loss was accompanied by an endothermic peak in the DSC profile occurring between 100–120 °C, see Supporting Information, Figure S8. The second weight loss (ca. 10%) for the same materials occurred between 150–550 °C, and the third weight loss (ca. 1%) was observed beyond 750 °C.

In addition to thermogravimetric analysis, the stability of the as-synthesized 10% multidoped OMS-2 materials in terms of phase changes was determined under oxidative (air) atmosphere. To do this, in-situ X-ray diffraction patterns were

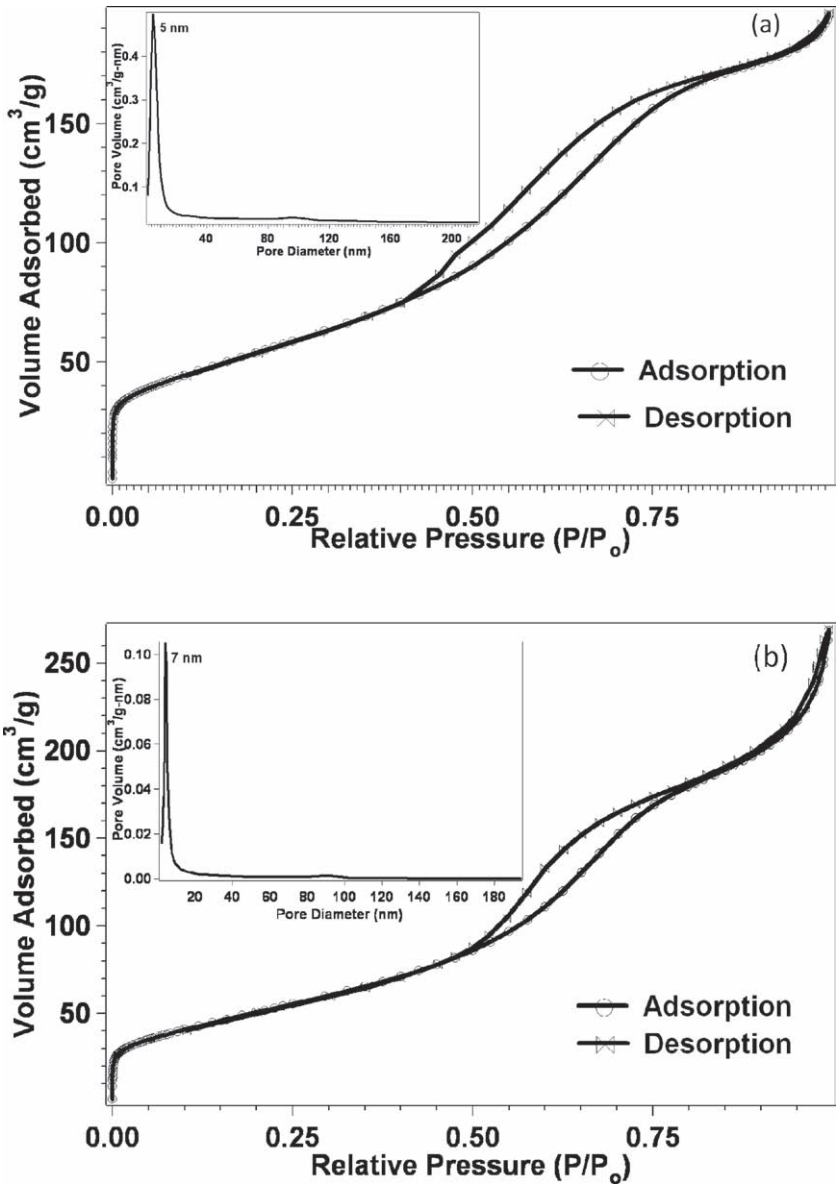

Figure 9. N_2 adsorption/desorption isotherms for a) 10% multidoped OMS-2 prepared with acid, b) 10% multidoped OMS-2 prepared without acid. The insets are pore-size distributions calculated by the BJH method from the respective adsorption branches.

acquired at different temperatures. From **Figure 11**, it can be seen that the cryptomelane phase of the as-synthesized materials was stable up to 450 °C, however, above this temperature, new phase(s) were formed that could probably be attributed to a mixture of manganese and dopant metal oxides.

2.8. Catalytic Studies

Cryptomelane-type manganese oxide octahedral molecular sieves (OMS-2) have been explored as catalysts in a number of processes, for instance, in the selective oxidation of alcohols,[37] and 9H-fluorene,[38] as well as in the synthesis of useful organic compounds such as 2-aminodiphenylamine,[39] among others. The catalytic performance of the 10% multidoped OMS-2 nanomaterials prepared with and without nitric acid was examined in the oxidation of diphenylmethanol to diphenylmethanone according to literature procedures reported by Son et al.[40]

The recyclability of the catalyst was tested by carrying out the diphenylmethanol oxidation reaction over five cycles using the same catalyst, which was regenerated by washing with acetonitrile/methanol then water and dried at 200 °C overnight after each use. As the whole catalyst could not be recovered after each reaction, a reduced amount of catalyst was used in the subsequent cycles. As shown in **Table 3**, the as-synthesized 10% multidoped OMS-2 materials showed 100% conversion and selectivity towards diphenylmethanone as opposed to the 35% conversion reported in the literature for the regular OMS-2.[40] The yields of the recycled catalyst in all the cycles on the other hand were comparable to the yields for the fresh catalyst, taking into account the loss of catalyst after recycling (the yield of the reduced amount of recycled catalyst was compared to the yield of the same amount of fresh catalyst). In order to prove that the catalyst structure is stable after recycling, X-ray diffraction patterns were taken after the fourth cycle. No significant structural changes were observed in the used catalyst, see Supporting Information, Figure S9.

3. Discussion

3.1. Multiple Substitutions into the Octahedral Molecular Sieves (OMS-2) Structure

The increase in the crystallite size of the multidoped OMS-2 material when either Fe, Cu, V, or Mo were omitted from the recipe (Figure 4) confirms that multiple substitutions/doping into the OMS-2 structure are possible without compromising its crystalline structural integrity. If one of the dopants was not being incorporated into the OMS-2 structure, the crystallite size would not change when it was omitted.

In order to elucidate the manner in which the OMS-2 structure was multidoped, we considered the mechanism of charge balance in the regular (undoped) K-OMS-2, and the mechanism through which each metal cation (Fe^{2+}, Cu^{2+}, V^{5+}, and Mo^{6+}) is inserted into the structure in a single-doping scenario. In regular OMS-2, the charge balance described by Feng et al.[41] as 'coupled cryptomelane exchange' is represented by

$$^{VIII}\square^{0} + {}^{VI}Mn^{4+} \leftrightarrow {}^{VIII}K^{1+} + {}^{VI}Mn^{3+} \quad (1)$$

Table 1. Textural properties of multidoped OMS-2 materials.

Sample	S_{BET} [m^2 g^{-1}][a)]	Pore Size [nm][b)]	Pore Volume [cm^3 g^{-1}]	
			V_{micro}[c)]	V_{meso}[d)]
10%-MdS[e)]	380	5	0.0203	0.235
10%-MdS[f)]	367	7	0.0193	0.386
MdS-No-Cu	256	4	0.0064	0.284
MdS-No-Fe	268	4	0.0060	0.304
MdS-No-V	251	5	0.0066	0.319
MdS-No-Mo	206	12	0.0015	0.277

[a)]Total surface area of a sample based on the BET method. [b)]The most probable mesopore size based on the BJH method. [c)]Micropore volume (<2nm) based on the *t*-plot method. [d)]Mesopore volume (2–5 nm) based on the BJH method. [e)]10% multidoped OMS-2 material prepared with acid. [f)]10% multidoped OMS-2 material prepared without acid. MdS-2-No-X = multidoped OMS-2 material without X metal, where X = Mo, V, Fe, and Cu.

where $^{VIII}\square^{0}$ represents a vacant VIII-fold tunnel site, and maintains the structural integrity.

In doped OMS-2 materials, this charge balance upon substitution of dopant cation(s) for the three-valent (Mn^{3+}) or four-valent manganese (Mn^{4+}), is maintained either by a coupled substitution with an octahedral vacancy, or by the reduction of the net negative charge on the framework arising from the exchange of an Mn^{4+}- O^{2-} pair for an Mn^{3+} -OH^{-} ''reduced valent oxygen species' pair, as illustrated by Equation 2.

$$^{VI}Mn^{4+} + O^{2-} \leftrightarrow {}^{VI}Mn^{3+} + OH^{-} \quad (2)$$

Doping into the OMS-2 structure occurs in the octahedral framework and/or in the tunnels, as governed by the crystal radii and the coordination of the dopant cations.[42] For the dopant cation to substitute Mn in the octahedral framework, such cations must allow six-coordination and have a crystal radius (CR) almost the same size as that of $^{VI}Mn^{3+}$ low spin (LS) (0.72 Å), $^{VI}Mn^{3+}$ high spin (HS) (0.785 Å), and $^{VI}Mn^{4+}$ (0.67 Å), whereas for the dopant cation to go into the tunnel, such cations must allow eight-coordination and have a crystal radius almost the same size as that of K^{+} (1.65 Å). Based on this rationale, the six-coordinated, 5-valent vanadium (CR $^{VI}V^{5+}$ = 0.68 Å) and the six-coordinated, 6-valent molybdenum (CR $^{VI}Mo^{6+}$ = 0.83 Å) cations were therefore doped into the framework by the coupled exchange of a $^{VI}V^{5+}$–$^{VI}Mn^{3+}$ pair with $2^{VI}Mn^{4+}$ ions and a $^{VI}Mo^{6+}$–octahedral vacancy pair for $2^{VI}Mn^{3+}$, as shown by Equations 3 and 4, respectively.

$$^{VI}Mn^{3+} + {}^{VI}V^{5+} \leftrightarrow 2\,{}^{VI}Mn^{4+} \quad (3)$$

$$^{VI}M_{0}^{6+} + {}^{VI}\square^{0} \leftrightarrow 2^{VI}\,Mn^{3+} \quad (4)$$

The six-coordinated Fe^{3+}cations (CR $^{VI}Fe^{3+}$ = 0.69 Å) on the other hand were doped into the framework via the reduction of the net negative charge on the framework caused by the exchange of an Mn^{4+}–O^{2-} pair for an Mn^{3+} –'OH^{-} reduced valent oxygen species. This exchange can be described by coupling Fe-variants of cryptomelane and manganite exchanges shown by Equations 5 and 6, respectively.

$$^{VIII}\square^{0} + 2^{VI}\,Mn^{4+} + O^{2-} \leftrightarrow {}^{VI}Fe^{3+} + {}^{VI}Mn^{3+} + {}^{VIII}K^{1+} + OH^{-} \quad (5)$$

$$^{VIII}\square^{0} + 2^{VI}\,Mn^{4+} + O^{2-} \leftrightarrow 2\,{}^{VI}Fe^{3+} + {}^{VIII}K^{1+} + OH^{-} \quad (6)$$

The partial substitution of the tunnel K^{+} cations for the six-coordinated Cu^{2+} cations (CR $^{VI}Cu^{2+}$ = 0.87 Å) on the other hand can be explained by a variant of the 'coupled cryptomelane exchange', where $^{VI}Cu^{2+}$ cations are exchanged with framework $^{VI}Mn^{4+}$ as shown by Equation 7.

$$2\,{}^{VIII}\square^{0} + {}^{VI}Mn^{4+} \leftrightarrow 2^{VIII}\,K^{1+} + {}^{VI}Cu^{2+} \quad (7)$$

3.2. Effects of the Reaction Parameters on the Crystallization of the Multidoped OMS-2 Materials

The acidity of the reaction mixture, the total amount of dopants, and the refluxing time exerted a dramatic influence on the crystallization of the multidoped OMS-2. When both 10% and 15% multidoped OMS-2 were synthesized without nitric acid, a significant increase in peak intensities was observed (Figure 2). At 15% (w/w) total dopant level, the sample prepared with nitric acid was amorphous (Figure 2a), whereas that prepared without

Table 2. Energy dispersive X-ray analysis (EDAX) data for K-OMS-2 and 10% multidoped OMS-2 materials.

Sample	Spot	Atomic weight percentage [%]					
		Mo	V	Fe	Cu	Mn	K
10%-MdS[a)]	1	2.585	2.585	5.364	1.135	84.362	3.749
	2	3.304	2.801	4.804	0.928	84.708	3.455
	3	2.981	2.636	5.048	0.731	84.869	3.736
	4	3.182	2.556	5.293	0.748	84.626	3.599
K-OMS-2	1					93.699	6.301
	2					92.646	7.354
	3					92.612	7.388
	4					93.858	6.142

[a)]10% multidoped OMS-2 material prepared for 24 h at 100 °C without acid.

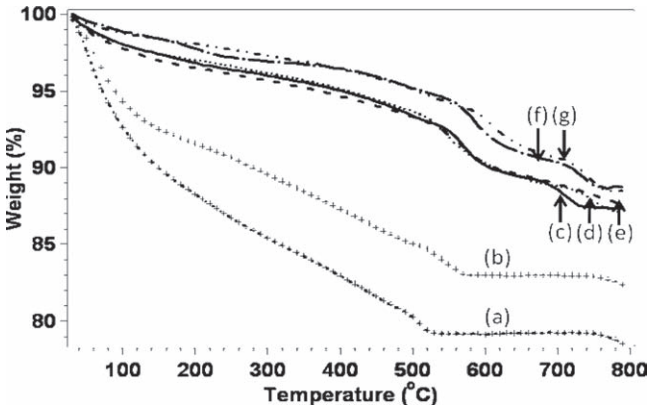

Figure 10. Thermogravimetric analysis profiles of a) 10% multidoped OMS-2 prepared without acid, b) 10% multidoped OMS-2 prepared with acid, c) 5% Cu-OMS-2, d) 5% Mo-OMS-2, e) 5% V-OMS-2, f) 5% Fe-OMS-2, and g) regular K-OMS-2. Reaction conditions: 24 h refluxing time at 100 °C.

the acid at the same doping level showed very broad peaks characteristic of the pristine cryptomelane phase (Figure 2b).

A rather more conspicuous change in peak intensity was observed in the 10% multidoped sample synthesized without the acid (Figure 2d), as compared to the one synthesized with the acid (Figure 2c). From an inorganic point of view Fe^{2+}, Cu^{2+}, V^{5+}, and Mo^{6+} ions are hard acids and thus their presence together—in levels permissible for framework/tunnel substitution and charge balance—presents an optimally strong oxidizing environment that is more favorable for the formation of cryptomelane crystals. However, when nitric acid is added into the reaction mixture, its oxidizing power coupled with that of the dopant ions (Fe^{2+}, Cu^{2+}, V^{5+}, and Mo^{6+}) furnishes an oxidizing environment that is so strong that the crystal growth of the multidoped OMS-2 is slowed down or hindered.

The total amount of dopants, on the other hand, was found to have a profound effect on the crystallinity of the multidoped OMS-materials (Figure 3). When the total amount of dopants

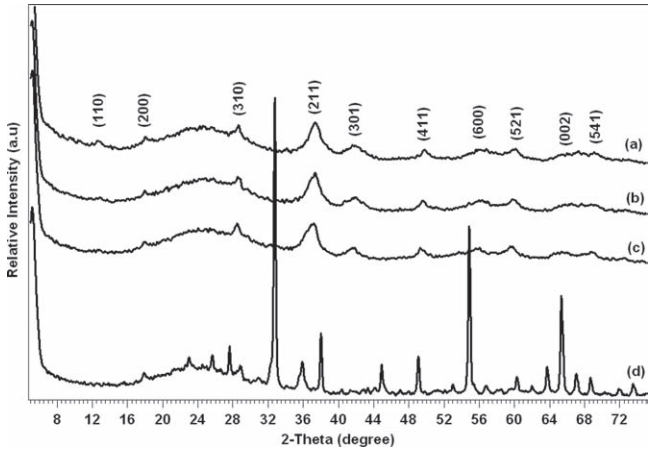

Figure 11. In-situ X-ray diffraction patterns of 10% multidoped OMS-2 material prepared with acid, a) at 100 °C, b) at 200 °C, c) at 450 °C, and d) at 550 °C.

was increased from 10% to 15%, a marked decrease in the XRD peak intensity and broadening of their widths was observed (Figure 3b). Increasing the total amount of dopants from 10% to 15% (w/w) led to the incorporation of more Mo, Cu, Fe, and V cations into the OMS-2 structure. Consequently, the multidoped OMS-2 crystallite size decreased as shown by the less intense and broad XRD peaks, (Figure 3b). When the total amount of dopants was increased past 15%, further incorporation of Mo, Cu, Fe, and V cations beyond the maximum allowable structural substitution limit of cryptomelane occurred, leading to the disruption of the charge balance that maintains the structural integrity of the OMS-2. This disruption was manifested by the breakdown of the OMS-2 crystalline structure and the consequent formation of amorphous material (Figure 3a).

3.3. Effects of the Multiple Substitutions on the OMS-2 Lattice Vibrations

Upon substitution of Mn in the local octahedral OMS-2 framework by other isomorphous metal ions, the local environment of oxygen coordination around the octahedral site changed along with the masses of the lattice vibrators and, hence, also the bond length/force constant. Consequently, the lattice vibrational behavior and spectral features of the bulk OMS-2 material change such that the peak positions shift and/or the peak intensities are attenuated or enhanced.[19,20] Because of the sensitivity of FTIR spectroscopy towards lattice vibrational changes, this technique was used to probe the effect of multiple substitution(s) on the spectral features of cryptomelane. The FTIR spectrum of the as-synthesized 10% multidoped OMS-2 material, Figure 7a, shows the dramatic spectral changes that occurred when the regular OMS-2 material, Figure 7b, was multidoped.

The enhancement of the intensity of the peak at 590 cm^{-1} as well as the attenuation of the intensity of the peak at 470 cm^{-1} observed after multidoping attest to lattice vibrational changes. As the MnO_6 octahedra are the main lattice vibrators (not tunnel cations) contributing to the spectral features exhibited by the hollandite group,[43] to which OMS-2 belongs, the observed spectral changes were ascribed to change(s) in the mass of the lattice vibrators arising from the successful insertion/doping of the Fe, V, and Mo cations into the OMS-2 octahedral framework. However, an unequivocal assignment of the observed spectral changes (the enhancement and attenuation of the peak intensities) to a particular metal dopant cation(s) is hard at this stage. This assignment will be pursued in our succeeding studies. The FTIR absorption bands at 720 cm^{-1}, 590 cm^{-1}, and 470 cm^{-1} for the regular OMS-2 material can be ascribed to the Mn-O lattice vibrations of the MnO_6 octahedra framework.[11]

The regular OMS-2 (cryptomelane) belongs to the $I4/m$ space[24] and using Factor group analysis,[30] the following irreducible representations (without tunnel cations contribution) can be attributed to the Mn-O lattice vibrations within the MnO_6 octahedral double chain:

$$\Gamma = 6A_g + 6B_g + 3E_g + 2A_u + 3B_u + 5E_u \quad (8)$$

Table 3. Oxidation of diphenylmethanol with 10% multidoped OMS-2 and catalyst reusability. Reaction conditions: 1.0 mmol of diphenylmethanol and catalysts were stirred in 10.0 mL toluene at 110 °C for 4 h.

Catalyst	Morphology	Cycle	Catalyst amount [mg]	Conversion [%][a)]	Selectivity [%][a)]
MdS-2[b)]	Microspheres[c)]	1	50	96{100}	100
		2	40	56{58}	100
		3	30	51{59}	100
		4	20	45{42}	100
		5	10	24{28}	100
K-OMS-2	Nanorods[c)]	1	50	35[d)]	100

[a)]Product identified and quantified by GC-MS; {Yield with fresh catalyst}. [b)]10% multidoped OMS-2 prepared without acid. [c)]Morphology of the "fresh" catalyst as determined by FESEM. [d)]Conversion reported by Son et al.[40]

where the A_g, B_g, and E_g (double-degenerated) modes are Raman active, the A_u and E_u (double-degenerated) modes are IR active, and the B_u mode is silent. The Raman spectrum obtained for the regular OMS-2 material only shows six Raman peaks at around 750 cm^{-1}, 650 cm^{-1}, 580 cm^{-1}, 520 cm^{-1}, 480 cm^{-1}, and 380 cm^{-1} as opposed to fifteen peaks predicted from Factor group analysis. This was caused by the low polarizabilities of some of these modes and low resolution of other modes.[30]

The two strong, sharp peaks at 650 cm^{-1} and 580 cm^{-1} correspond to A_{1g} spectroscopic modes whereas the peaks at 520 cm^{-1} and 480 cm^{-1} correspond to the F_{2g} spectroscopic species.[11] The two sharp peaks at 650 cm^{-1} and 580 cm^{-1} are associated with Mn-O vibrations that are orthogonal and along the direction of the MnO_6 octahedral double chains, respectively, and are indicative of a well-developed tetragonal structure with 2×2 tunnels.[31]

On the other hand, the Raman spectrum of the 10% multidoped OMS-2 material did not show the peaks at around 990 cm^{-1} and 818–876 cm^{-1} corresponding to Mo=O and O-Mo-O stretching vibrations, respectively,[32] suggesting that there was no detectable free molybdenum oxide (MoO_3) present. Symmetric vibrations due to vanadyl bonds (V=O), which occur at around 993 cm^{-1} in free vanadium pentoxide (V_2O_5),[33] were also not observed, see Figure 8a. Also, there were no Raman peaks at around 1323 cm^{-1} and 290 cm^{-1} corresponding to segregated Fe_2O_3 and CuO, respectively.[34,35] In general, the Raman data depicted the absence of segregated metal oxide impurities, and, therefore, corroborates the FTIR and the XRD data, which showed no extra peaks for segregated metal oxide(s).

3.4. Morphology and Particle Size

The regular OMS-2 material prepared by the reflux method showed a homogeneous fibrous morphology, see the inset of Figure 5a. This is quintessentially the morphology of the OMS-2 materials synthesized by the reflux route.[11,18] Upon multidoping, a fibrous morphology was not obtained, instead the multidoped OMS-2 materials prepared with or without nitric acid crystallized into a flake-like morphology, see the inset of Figure 5b. The TEM images (Figure 6b,c, and Figure S3) confirmed the flake-like morphology observed in the FESEM studies.

During the crystallization process of the undoped synthetic OMS-2 material the crystal growth in the *c*-direction[30] leads to the formation of a fibrous/nanorod material with 1×1 and 2×2 tunnels running along the length of the nanofibres/nanorods. The formation of the flake-like morphology in our multidoped materials was probably due to a slight distortion of the tetragonal crystal structure of cryptomelane to the monoclinic geometry. Crystal growth along the *c*-axis of the monoclinic structure as shown schematically in Figure 1a then led to the formation of flake-like particles where the tunnels run along the shortest *b*-direction of a monoclinic unit cell, which in our material corresponds to the thickness of the flakes.

Based on the work of Post et al.[44] wherein the ideal tetragonal unit cell ($I4/m$) is reported to undergo a small structural distortion that lowers the symmetry to the monoclinic space group $I2/m$ when large cation(s), for instance Mo^{6+} cations in our materials, substitute octahedral Mn^{4+} and/or Mn^{+3} cations, or when relatively smaller cations, for example copper cations (Cu^{2+} = 0.87 Å) in our materials, substitute the tunnel potassium cations (K^+ = 1.65 Å). Substitution of small cations leads to the twisting of the octahedral framework and thus the formation of the monoclinic structure. The crystal structure distortion suggested in our work is therefore caused by the successful substitutions of the V, Mo, Fe, and Cu cations into the OMS-2 structure.

The hollow microspheres (Figure 5 and Figure S2 in the Supporting Information) arise from template-free, physical stacking of the pseudo-flakes driven by the interfacial/surface forces between the hydrophilic surfaces of the OMS-2 nanoparticles and the solvent employed.[9] The unambiguous observation of the 2×2 and 1×1 tunnels in the 10% multidoped OMS-2 material (Figure 6e), revealed by the HRTEM studies, was attributed to the flake-like morphology of our material. As the particles prefer orienting themselves with their longest dimensions parallel to the TEM grid, the most probable orientation of the regular fibrous OMS-2 material would be such that the length of the fiber(s) and, hence, the tunnels are parallel to the plane of the TEM grid, and thus the orientation is orthogonal to the electron beam as shown schematically in Figure 1b.

In contrast, the most probable orientation of flake(s) would be lying on *ac*-plane(s) on the grid, with the tunnels perpendicular to the grid but parallel to the TEM electron-beam direction as shown schematically in Figure 1a. The nanoflake orientation in Figure 6e was such that the tunnels were parallel to the beam and, therefore, the spectacular array of the tunnels in the as-synthesized 10% multidoped OMS-2 material could

be revealed. In addition to the morphology, the unprecedented observation of the tunnels was ascribed to the ultrafine nature (ca. 5.0 nm) of the flakes. As the particle size decreases, the number of ways (freedom of orientation) a particle can orient itself with respect to the electron-beam direction increases, and as such, the propensity of particle(s) orienting in a manner such that the tunnels are in line with the electron beam (so that they are observed) increases when the particle size decreases, and vice versa.

3.5. Surface Area and Pore Distribution

The 10% multidoped OMS-2 materials showed type-IV[45] N_2 adsorption/desorption isotherms (Figure 9) with H_2-type hysteresis loops typical for corpuscular (globe-like) particles.[46] The observed type-IV isotherms and H_2-type hysteresis loops confirm that the as-synthesized 10% multidoped OMS-2 materials are porous materials, with globular particles whose cavities are interconnected.[47]

The adsorption isotherms in the P/P_0 range below 0.45 for both 10% multidoped OMS-2 materials (prepared with and without acid) corresponded to formation of monolayers and multilayers of adsorbed molecules.[48] The path followed by the adsorption isotherms (at $P/P_0 < 0.45$) of our material is typical for micropore filling, and this suggests the presence of micropores in the 10% multidoped OMS-2 materials.[36] At relative pressures P/P_0 higher than 0.5, the adsorption isotherms showed a rapid increase in the volume of the adsorbed gas associated with the progressive filling of mesopores by capillary condensation.[48,49]

In contrast to the 10% multidoped OMS-2 materials, OMS-2 materials doped with three metal cations showed relatively longer hysteresis loops, whereby the OMS-2 material multidoped without Mo cation showed an H_3-type hysteresis loop[46] that occurred at high P/P_0 (close to saturation). This is indicative of slit-shaped mesopores with varying sizes and shape.[11,36] BJH average pore diameters of 5 and 7 nm (Figure 9a and 9b insets) confirm the mesoporous nature of the 10% multidoped OMS-2 materials. In addition to the narrow pore-size distribution around 7 nm, the 10% multidoped OMS-2 material prepared without acid showed a broad pore-size distribution around 85 nm, see Figure 9b inset. This is indicative of a minor macroporosity in this material which explains why the adsorption isotherm shown in Figure 9b increased more rapidly, compared to that in Figure 9a, instead of reaching a plateau at high P/P_0.

The Brunauer-Emmett-Teller (BET) surface areas of the 10% multidoped OMS-2 material prepared with and without nitric acid were found to be 380 and 367 $m^2\ g^{-1}$, respectively. These high surface areas, which are the highest reported for synthetic cryptomelane to date, were attributed to the small particle size (ca. 5.0 nm) of the material (Figure S3), the microporosity of the individual particles arising from the characteristic 1×1 and 2×2 tunnels of the cryptomelane materials, and the hollowness of the self-assembled microspheres, depicted by Figure S2 and 5d. The particle sizes calculated by the Debye–Scherer equation (ca. 5.0 nm) correlated well with those calculated from the HRTEM images, Figure S3.

3.6. Thermal Stability and Catalytic Application of the Synthesized Multidoped OMS-2 Materials

Thermogravimetric analysis (TGA) studies, Figure 10, show that the undoped OMS-2 material has a higher thermal stability than both the single- and multidoped OMS-2 materials, except for the Fe-doped OMS-2 material, which shows a thermal stability that is almost the same as that of the undoped OMS-2. These results are in agreement with the work of Calvert et al.,[24] who showed that the undoped OMS-2 material was more thermally stable than its tungstate-doped (W-OMS-2) material counterpart. Although 10% multidoped OMS-2 materials prepared with and without nitric acid, Figure 10b and 10a, respectively, showed a dramatic weight loss compared to the undoped and single-doped OMS-2 materials, the 10% multidoped material prepared without acid was found to be more thermally unstable than its counterpart prepared with acid. The low thermal stability exhibited by the 10% multidoped OMS-2 materials was possibly related to lattice vacancies created by the insertion of high[24] and low valent metal ions into the OMS-2 structure. In addition to lattice vacancies, the low thermal instability was probably caused by the structural/lattice constraints imparted by the slight crystal radii mismatch, as reported by Makwana et al.[39]

The first weight loss (ca. 7%) for the 10% multidoped OMS-2 materials observed between 35–120 °C in the TGA profiles, was accompanied by an endothermic peak in the DSC profile occurring between 100–120 °C (see Supporting Information, Figure S8). As this temperature is approximately the boiling point of water, this weight loss was ascribed to the loss of physisorbed water molecules on the surface of the materials.[11,16] Accompanying the second weight loss (ca. 10%) occurring between 150–550 °C, was an exothermic DSC peak at 350 °C.

The second weight loss was thus attributed to the loss of water molecules that were chemically bound in the OMS-2 structure,[11,16] whereas the third weight loss (ca. 1%) occurring beyond 750 °C was ascribed to the release of lattice oxygen.

The 10% multidoped OMS-2 materials appear to be more thermally unstable than their undoped and single OMS-2 counterparts (see TGA profiles, Figure 10). However, in-situ XRD shows that the cryptomelane phase of the 10% multidoped OMS-2 materials is stable up to about 450 °C, see Figure 11. This is consistent with the work of Chen et al.[36] that showed that the phase of single-doped OMS-2 materials changed at temperatures below 600 °C; the temperature at which the K-OMS-2 phase changed in air.

The synthesized 10% multidoped OMS-2 materials showed an excellent catalytic activity for the oxidation of diphenylmethanol to diphenylmethanone, Table 3. Previous diphenylmethanol oxidation work carried out by Son et al.[40] using undoped OMS-2 showed only a 35% conversion, whereas our materials showed 100% conversion under the same conditions of reaction temperature, reaction time, solvent, catalyst amount, and GC-MS quantification methods. The high catalytic activity of the as-synthesized 10% multidoped OMS-2 materials was attributed to their high BET surface area and their low lattice oxygen stability as opposed to their undoped and single-doped counterparts. This is in accordance with the work of Makwana et al.[37] on selective oxidation, where an increase in the OMS-2 catalytic

activity with increase in lattice instability was reported. The low lattice oxygen stabilities of the 10% multidoped materials are evident from the TGA profiles in Figure 10a and 10b.

Based on the work of Son et al.[40] where OMS-2 materials were reported to have a low catalytic activity towards bulky substrates, for instance 1-acenaphthenol, the active sites (in this case Mn^{3+} ions) of these materials (OMS-2) were inside the tunnels. Moreover, Opembe et al.[38] also suggested that small crystallites are more susceptible to fracturing thereby disrupting the tunnels and exposing more active sites.

The high catalytic activity of the 10% multidoped materials could thus be related to the high number of accessible active sites arising from the more exposed tunnels of the pseudo-nanoflakes (ca. 5 nm) as opposed to the lower number of exposed tunnels of the long nanofibers/rods in the K-OMS-2 samples. As diphenylmethanol molecules are as bulky as 1-acenaphthenol molecules,[40] and, therefore, can not go through the tunnels (which constitute the highest number of micropores in OMS- materials), the oxidation reaction is thought to occur outside the micropores, which in our material are more exposed because of the small crystallite size and flake-like morphology.

4. Conclusions

We have successfully demonstrated a facile route to tailoring the morphology, particle size, crystal system, surface area, and hence the chemical/physical properties of manganese oxide octahedral molecular sieves (OMS-2) via multiple substitutions of both low and high-valent metal ions into the cryptomelane structure. By this method, nanocrystalline multidoped OMS-2 materials with surface areas ranging from 367 to 380 $m^2\ g^{-1}$ and ultrafine particles of about 5.0 nm were synthesized. The ultrafine particles were obtained via multiple framework substitutions whereas the tertiary structures emanated from the physical stacking of the ultrafine primary structures into hollow microspheres with average diameters of 0.5 μm–2.0 μm. Multidoping therefore joins other known strategies for tailoring the morphology, particle size, and chemical properties of cryptomelane (OMS-2), such as the manipulation of temperature, pressure, and pH, as well as the use of co-solvents.

This strategy can therefore be extended to other manganese oxide octahedral sieves, for instance todorokite (OMS-1), and thus help in fabricating useful nanoscale devices and systems.

5. Experimental Section

Synthesis: In a typical synthesis, $MnSO_4.H_2O$ (4.4 g, 26.0 mmol) and concentrated HNO_3 (1.5 mL) were dissolved in deionized water (15.0 mL). Then a solution made by dissolving $KMnO_4$ (2.9 g, 18.4 mmol) in deionized water (40.0 mL) was added drop-wise to make a brown slurry. Finally, $CuSO_4.5H_2O$ (0.480 g, 1.9 mmol), $FeSO_4.7H_2O$ (0.608 g, 2.2 mmol), $MoNa_2O_4.2H_2O$ (0.307 g, 1.3 mmol), and $VOSO_4.x2H_2O$ (0.390 g, 2.4 mmol) dissolved in deionized water (10.0 mL) were added drop-wise and quantitatively into the slurry while stirring. The final dark brown slurry was then refluxed at 100–110 °C in a 250 mL round-bottom flask for 24 h. The product was washed with copious amounts of deionized water to remove unreacted precursors, filtered, and then dried at 120 °C overnight.

Characterization: X-ray powder diffraction (XRD) analysis was conducted on a Scintag Model PDS 2000 diffractometer with Cu Kα radiation ($\lambda = 1.5418$ Å). The particle size of the synthesized multidoped OMS-2 was calculated using the Debye-Scherrer equation,[28] with the integral widths corrected using a LaB_6 standard. Morphological studies were carried out using a Zeiss DSM 982 Gemini FESEM with a Schottky emitter operating at 2.0 kV with a beam current of 1.0 mA. Transmission electron microscopy (TEM) images were obtained using a FEI Tecnai T12 S/TEM and JEOL JEM 2010 FasTEM operating at 200 kV. The specimens were loaded onto a carbon-coated gold grid. The elemental analyses were carried out with an Amray model 1810D operated at 20.0 kV, with the X-ray spectra being acquired and processed with an Amray model PV 9800 EDS system.

Element concentrations were reported in atomic weight percentages (Table 2) and were computed by the ZAF method. The Brunauer-Emmett-Teller (BET) surface-area measurements were carried out using a Micromeritics ASAP 2010 accelerated surface-area system. Prior to the analysis, the samples were degassed at 200 °C for 12 h. Fourier-transform infrared (FTIR) spectra were obtained using a Nicolet Magna-IR system 560 FTIR spectrometer at room temperature. For FTIR, powdered specimens were diluted with KBr at a ratio of 1:100, and pressed into a pellet. The spectral background was collected using pure KBr discs. Raman measurements were taken at room temperature on a Renishaw 2000 Ramascope attached to a CCD camera, with an Ar^+ laser (514.4 nm) as the excitation source. Before each measurement was taken, the spectrometer was calibrated with a silicon wafer.

Thermogravimetric analysis (TGA) and differential scanning calorimetry (DSC) experiments were performed using a Hi-Res TA instrument Model 2950 and DSC Model Q100. The temperature ramp for both TGA and DSC was 20.0 ° C min^{-1} in nitrogen atmosphere.

Catalytic Studies: The diphenylmethanol was purchased from Fischer and used without any further purification. The oxidation reaction was carried out in batch mode, where 50.0 mg of the 10% multidoped OMS-2 catalyst, 1.0 mmol of diphenylmethanol, and 10.0 mL of toluene were charged into a three-necked 50 mL round flask and refluxed at 110 °C under air for 4 h. The identification and quantification of the reaction products was carried out by GC-MS, using a HP 5971 mass-selective detector coupled to a HP 5890 Series II gas chromatography through a HP-1 nonpolar cross-linked methyl siloxane column, with dimensions of 12.5 m × 0.2 mm × 0.33 μm.

Supporting Information

Supporting Information is available from the Wiley Online Library or from the author.

Acknowledgements

We thank the Chemical Sciences, Geosciences, and Biosciences Division of the Office of Basic Energy Sciences, Office of Science, U.S. Department of Energy for support of this research and Dr. Frank Galasso and Dr. Raymond Joesten for helpful discussions.

Received: May 20, 2010
Published online: November 25, 2010

[1] K. A. Malinger, Y. Ding, S. Sithambaram, L. Espinal, S. L. Suib, *J. Catal.* **2006**, *239*, 290.
[2] A. Corma, P. Atienzar, H. García, J.-Y. Chane-Ching, *Nat. Mater.* **2004**, *3*, 394.
[3] M. Tsuji, *Solvent Extraction and Ion Exchange* **2001**, *19*, 531.
[4] K. J. Euler, H. J. Mueller-Helsa, *J. Power Sources* **1979**, *4*, 77.

[5] T. Sasaki, S. Komaba, N. Kumagai, I. Nakai, *Electrochem. Solid-State Lett.* **2005**, *8*, A471.
[6] S. Sithambaram, R. Kumar, Y.-C. Son, S. L. Suib, *J. Catal.* **2008**, *253*, 269.
[7] R. Ghosh, X.-F. Shen, J. C. V. Y. Ding, K. Malinger, S. L. Suib, *J. Phys. Chem. B* **2006**, *110*, 7592.
[8] L. Li, P Yinzhen, C Lijuan, L. Guangshe, *J. Solid State Chem.* **2007**, *180*, 2896.
[9] J. Yuan, W.-N. Li, S. Gomez, S. L. Suib, *J. Am. Chem. Soc.* **2005**, *127*, 14184.
[10] J. Luo, H. T. Zhu, H. M. Fan, J. K. Liang, H. L. Shi, G. H. Rao, J. B. Li, Z. M. Du, Z. X. Shen, *J. Phys. Chem. C* **2008**, *112*, 12594.
[11] E. K. Nyutu, C.-H. Chen, S. Sithambaram, V. M. B. Crisostomo, S. L. Suib, *J. Phys. Chem. C* **2008**, *112*, 6786.
[12] O. Giraldo, M. Marquez, S. L. Brock, S. L. Suib, H. Hillhouse, M. Tsapatsis, *J. Am. Chem. Soc.* **2000**, *122*, 12158.
[13] S. Ching, E. J. Welch, S. M. Hughes, A. B. F. Bahadoor, S. L. Suib, *Chem. Mater.* **2002**, *14*, 1292.
[14] S. Ching, J. L. Roark, N. Duan, S. L. Suib, *Chem. Mater.* **1997**, *9*, 750.
[15] Z. Li, Yue Ding, Y. Xiong, Q. Yang, Y. Xie, *Chem. Commun.* **2005**, 918.
[16] J. C. Villegas, L. J. Garces, S. Gomez, J. P. Duran, S. L. Suib, *Chem. Mater.* **2005**, *17*, 1910.
[17] L.-X. Yang, Y.-J. Zhu, W.-W. Wang, H. Tong, M.-L. Ruan, *J. Phys. Chem. B* **2006**, *110*, 6609.
[18] R. Kumar, S. Sithambaram, S. L. Suib, *J. Catal.* **2009**, *262*, 304.
[19] A. M. A. Hashem, H. A. Mohamed, A. Bahloul, A. E. Eid, C. M. Julien, *Ionics* **2008**, *14*, 7.
[20] J. Cai, J. Liu, W. S. Willis, S. L. Suib, *Chem. Mater.* **2001**, *13*, 2413.
[21] Z. Liu, Y. Xing, C.-H. Chen, L. Zhao, S. L. Suib, *Chem. Mater.* **2008**, *20*, 2069.
[22] S. Ching, P. F. Driscoll, K. S. Kieltyka, M. R. Marvel, S. L. Suib, *Chem. Commun.* **2001**, 2486.
[23] R. Jothiramalingam, B. Viswanathan, T. K. Varadarajan, *J. Mol. Catal. A: Chem.* **2006**, *252*, 49.
[24] C. Calvert, R. Joesten, K. Ngala, J. Villegas, A. Morey, X.-F. Shen, S. L. Suib, *Chem. Mater.* **2008**, *20*, 6382.
[25] M. Polverejan, J. C. Villegas, S. L. Suib, *J. Am. Chem. Soc.* **2004**, *126*, 7774.
[26] W.-N. Li, J. Yuan, X.-F. Shen, S. G.-Mower, L.-P. Xu, S. Sithambaram, M. Aindow, S. L. Sui, *Adv. Funct. Mater.* **2006**, *16*, 1247.
[27] T. Sriskandakumar, N. Opembe, C.-H. Chen, A. Morey, C. King'ondu, S. L. Suib, *J. Phys. Chem. A* **2009**, *113*, 1523.
[28] a) H. Klug, L. Alexander, *X-ray Diffraction procedures*, Wiley, New York, NJ **1962**, p. 125; b) B. D. Cullity, S. R. Stock, *Elements of X-Ray Diffraction*, Prentice Hall, Upper Saddle River, NJ **2001**, p. 170.
[29] CrystalMaker: A crystal and molecular structure program for mac and windows. CrystalMaker Software Ltd, Oxford UK; www.crystalmaker.com, Version 2.1.5 1994-2009.
[30] T. Gao, M. Glerup, F. Krumeich, R. Nesper, H. Fjellvåg, P. Norby, *J. Phys. Chem. C* **2008**, *112*, 13134.
[31] R. M. Potter, G. R. Rossman, *Am. Mineral.* **1979**, *64*, 1199.
[32] L. Seguin, M. Figlarz, R. Cavagnat, J.-C. Lasskgues, *Spectrochim. Acta A* **1995**, *51*, 1323.
[33] C. V. Ramana, R. J. Smith, O. M. Hussain, M. Massot, C. M. Julien, *Surf. Interface Anal.* **2005**, *37*, 406.
[34] A. G. Nasibulin, S. Rackauskas, H. Jiang, Y. Tian, P. R. Mudimela, S. D. Shandakov, L. Nasibulina, J. Sainio, E. I. Kauppinen, *Nano Res.* **2009**, *2*, 373.
[35] D. Chen, G. Shen, K. Tang, Y. Qian, *J. Cryst. Growth* **2003**, *254*, 225.
[36] X. Chen, Y.-F. Shen, C. L. O'Young, S. L. Suib, *Chem. Mater.* **2002**, *14*, 940.
[37] V. D. Makwana, L. J. Garces, J. Liu, J. Cai, Y.-C. Son, S. L. Suib, *Catal. Today* **2003**, *85*, 225.
[38] N. N. Opembe, Y.-C. Son, T. Sriskandakumar, S. L. Suib, *ChemSusChem* **2008**, *1*, 182.
[39] R. Kumar, L. J. Garces, Y.-C. Son, S. L. Suib, *J. Catal.* **2005**, *236*, 387.
[40] Y.-C Son, V. D. Makwana, A. R. Howell, S. L. Suib, *Angew. Chem. Int. Ed.* **2001**, *40*, 22.
[41] Q. Feng, H. Kanoh, Y. Miyai, K. Ooi, *Chem. Mater.* **1995**, *7*, 148.
[42] a) R. D. Shannon, *Acta Crystallogr.* **1976**, *A32*, 751; b) R. D. Shannon, C. T. Prewitt, *Acta Crystallogr.* **1969**, *B25*, 925.
[43] C. M. Julien, M. Massot, C. Poinsignon, *Spectrochim. Acta A* **2004**, *60*, 689.
[44] J. E. Post, R. B. Von Dreele, P. R. Buseck, *Acta Crystallogr.* **1982**, *B38*, 1056.
[45] K. W. Kolasinski, in *Foundations of Catalysis and Nanoscience*, 2nd ed., John Wiley and Son, West Sussex, UK**2008**, p. 236.
[46] S. J. Gregg, K. S. W. Sing, in *Adsorption, Surface Area and Porosity*, 2nd ed., Academic Press, London **1982**, p. 287.
[47] A.Grosman, C. Ortega, *Langmuir* **2008**, *24*, 3977.
[48] A. Dias, V. S. T. Ciminelli, *Ferroelectrics* **2000**, *241*, 9.
[49] L. Benhaddad, L. Makhloufi, B. Messaoudi, K. Rahmouni, H. Takenouti, *Appl. Mater. Interfaces* **2009**, *1*, 424.